Taylor & Francis
Taylor & Francis Group

Check for updates

Triangular prismatic solid-shell element with generalised deformation description

Vicente Mataix[a] (ID), Fernando G. Flores[b,c] (ID), Riccardo Rossi[a] (ID) and Eugenio Oñate[a] (ID)

[a]CIMNE (Centre Internacional de Mètodes Numèrics en Enginyeria). Edificio C1 Campus Nord, UPC, Barcelona, Spain; [b]Department of Structures, Universidad Nacional de Córdoba and CONICET, Córdoba, Argentina

ABSTRACT

The solid-shells are an attractive kind of element for the simulation of forming processes, due to the fact that any kind of generic 3D constitutive law can be employed without any kind of additional modification, besides the thermomechanic problem is formulated without additional assumptions. Additionally, this type of element allows the three-dimensional description of the deformable body, thus contact on both sides of the element can be treated easily. The present work consists in the development of a triangular prism element as a solid-shell, for the analysis of thin/thick shell, undergoing large deformations. The element is formulated in total Lagrangian formulation, and employs the neighbour (adjacent) elements to perform a local patch to enrich the displacement field. In the original formulation by Flores, a modified right Cauchy-Green deformation tensor ($\bar{C}$) is obtained; in the present work a modified deformation gradient ($\bar{F}$) is obtained, which allows to generalise the methodology and allows to employ a wide range of constitutive laws. The element is based in three modifications: (a) a classical assumed strain approach for transverse shear strains (b) an assumed strain approach for the in-plane components using information from neighbour elements and (c) an averaging of the volumetric strain over the element. The objective is to use this type of elements for the simulation of shells avoiding transverse shear locking, improving the membrane behaviour of the in-plane triangle and to handle quasi-incompressible materials or materials with isochoric plastic flow. Some examples have been evaluated to show the good performance of the element and results.

1. Introduction

Solid-shells have been during the last 15 years (de Sousa, Cardoso, Valente, Yoon, Grácio, & Jorge, 2005; Dvorkin & Bathe, 1984; Hauptmann, Doll, Harnau, & Schweizerhof, 2001; Hauptmann & Schweizerhof, 1998; Hauptmann, Schweizerhof, & Doll, 2000; Klinkel, Gruttmann, & Wagner, 2006; Parente, Valente, Jorge,

---

CONTACT Vicente Mataix ✉ vmataix@cimne.upc.edu

Cardoso, & de Sousa, 2006) an important improvement in the shells simulations, providing a reliable simulations and avoiding the problematic that are associated to the kinematics hypothesis and plane stress constitutive laws related to the use of the shell element (or any kind of bidimensional elements as plates and membranes). The main advantages when using **solid-shell** elements are: (a) general 3D constitutive relations; (b) large transverse shear can be considered, and considering additional elements along the thickness improve this behaviour; (c) there is no need to consider transitions between solid and shell elements (all the elements are solids); (d) contact forces can be introduced directly in the geometry and in a realistic way without any additional technique, which is especially important for the consideration of friction; (e) the element is **rotation-free**, avoiding the storage and computation of this variables; (f) in the case where we have non-parallel boundaries this can be modelled correctly.

For the consideration of strongly non-linear problems, problems where the contact-friction, large deformations and complex constitutive laws are considered, the use of low interpolation order elements is preferred. Most of the existing **solid-shells** are linear hexahedron (Abed-Meraim & Combescure, 2009; de Sousa et al., 2005; Dvorkin & Bathe, 1984; Hauptmann & Schweizerhof, 1998; Hauptmann et al., 2000, 2001; Klinkel, Gruttmann, & Wagner, 2006; Parente et al., 2006; Schwarze & Reese, 2011; Schwarze, Vladimirov, & Reese, 2011; Sena, Alves de Sousa, & Valente, 2011; Sena et al., 2016) (usually tri-linear 8-node brick), which have two main disadvantages; the first one is the *hourglass* effect, which is called this way due to the characteristics shapes adopted in the proper modes and a stabilisation is required to reduce this problems; the second problematic is the meshing of the plane, due to the fact that meshing quadrilateral is less performant than triangles. For this reasons, the triangular prisms (wedges) could be considered an interesting alternative (Flores, 2013a, 2013b), specially for the second problem mentioned, but this kind of geometry is not exempt of problematic, owing to the low order of interpolation of the geometry, when a linear triangular prism is considered. This last problem can be solved with the consideration of the neighbours elements,[1] in consequence the element becomes quadratic in the plane solving this last problem. Additionally some recent works (Wang, Chalal, & Abed-Meraim, 2016) consider both quadratic wedge and hexaedron in order to tackle the locking problems that appear in the linear elements, but these kind of elements carry their own discussion between accuracy and computational cost, among practical reasons.

In addition to this, it is well know that low interpolation order elements in the standard displacement formulation (in contract to the mixed formulation) in the consideration of slender structures and incompressible materials suffer severe locking effects. The *transverse shear locking* provokes problems in the bending behaviour, especially when more slender is the element. The *membrane locking appears* especially in the initially curved shells when bending is preponderant without middle surface stretching. A *curvature thickness locking* can appear in

problems with initially curved geometry due to artificial transverse strains and stresses under pure bending. Finally, the *volumetric locking* can appear when the material present an incompressible, nearly incompressible behaviour or elastic–plastic materials with isochoric plastic flow (typical in metals).

The content of this proceeding will be the following one: (1) The theory concerning to the element is presented, (2) Some test cases are presented to show the good performance of the element, (3) complementary information is presented in the Appendix 1 for a better understanding of the theory.

The element has been implemented into *Kratos* (Dadvand, Rossi, Oñate, 2010), the in-home **FEM-Multiphysics** open-source code, implemented in C++ with parallelization capabilities. The pre/post-process of allthe presented examples haven been processed with *GiD* (Ribó, Pasenau, Escolano, Ronda, user manual), the *CIMNE* software for pre- and post-processing.

2. Theory

2.1. Basic kinematics of the standard element

We can found the standard isoparametric interpolations for the linear 6-node triangular prism (or wedge) in (1), where $\mathbf{X}^I$, $\mathbf{x}^I$ and $\mathbf{u}^I$ correspond with the original coordinates (or undeformed configuration), the current coordinates (or deformed configuration) and the displacements in the node I respectively.

$$\mathbf{X}(\xi) = \sum_{I=1}^{6} N^I(\xi)\mathbf{X}^I \tag{1a}$$

$$\mathbf{x}(\xi) = \sum_{I=1}^{6} N^I(\xi)\mathbf{x}^I = \sum_{I=1}^{6} \left(\mathbf{X}^I + \mathbf{u}^I\right) \tag{1b}$$

The shape functions $N^I(\xi)$ from (2) are defined in function of the local coordinates (ξ, η, ζ), where the two first define the position in the plane of the triangular base and the third one corresponds with the coordinate along the prism axis.

$$\begin{aligned} N^1 = zL^1, N^2 = \xi L^1, N^3 = \eta L^1 \\ N^4 = zL^2, N^5 = \xi L^2, N^3 = \eta L^2 \end{aligned} \tag{2a}$$

In this definition the third triangular coordinate and the axis interpolation is defined as:

$$z = 1 - \xi - \eta, L^1 = \tfrac{1}{2}(1 - \zeta), L^2 = \tfrac{1}{2}(1 + \zeta) \tag{2b}$$

We can define following the standard formulation the *Jacobian* matrix at each integration point as (7a), in consequence we can compute the *Cartesian* derivatives of the shape functions. At each element centre a local *Cartesian* triad can be defined as in (3b), that allows to compute the *Cartesian* derivatives with respect to this local system following the orthotropy directions.

$$\mathbf{J} = \frac{\partial \mathbf{X}}{\partial \xi} \rightarrow N_X^I = \mathbf{J}^{-1} N_\xi^I \tag{3a}$$

$$\mathbf{R} = \begin{bmatrix} \mathbf{t}_1, \mathbf{t}_2, \mathbf{t}_3 \end{bmatrix} \rightarrow N_Y^I = \mathbf{R}^T N_X^I \tag{3b}$$

As it will be shown in the following section, the left *Cauchy* tensor $\mathbf{C}$ is modified into the $\bar{\mathbf{C}}$ using the assumed strain techniques that in one case includes an additional internal degree of freedom α, leading to the improved tensor $\bar{\mathbf{C}}$. The balance equation to solve in the strong form for a **Total Lagrangian**[2] framework in **large strain** hypothesis is (4). Where $\mathbf{S}$ is the second *Piola-Kirchoff* stress tensor (**PK2**).

$$\begin{cases} g_1(\mathbf{u}, \alpha) = \int_{V_0} \frac{1}{2} \mathbf{S}(\bar{\mathbf{C}}) : \delta_u \bar{\mathbf{C}} dV_0 + g_e xt = 0 \\ g_2(\mathbf{u}, \alpha) = \int_{V_0} \frac{1}{2} \mathbf{S}(\bar{\mathbf{C}}) : \delta_\alpha \bar{\mathbf{C}} dV_0 + g_e xt = 0 \end{cases} \tag{4}$$

2.2. Modifications of the standard element

The prism presented in the previous lines corresponds with the standard, and it need to be modified for the sake of large strain elastic–plastic analysis of shells. For this purpose, different modifications are introduced in the metric tensor $\mathbf{C}$. The discretisation to be introduced in the prism solid-shell can be defined in first place with the discretisation of the triangular middle surface and in second place with the discretisation along the thickness. We will assume that the upper and lower face are almost parallel and thus the normal direction can be defined in function of ζ. In (5), the right *Cauchy-Green* tensor is decomposed according to the different behaviours that define classically the shells elements, this means we decompose in-plane (membrane and bending behaviour), transverse shear and normal components. The calculation of each one of the different components will be detailed in the next sections.

$$\mathbf{C} = \begin{bmatrix} C_{11}^m & C_{12}^m & C_{13}^s \\ C_{21}^m & C_{22}^m & C_{23}^s \\ C_{31}^m & C_{32}^m & C_{33}^n \end{bmatrix} \tag{5a}$$

where the index m, s and n mean membrane, shear and normal behaviour, respectively. In consequence, this tensor can be decomposed in three components as detailed in (5b).

$$\bar{\mathbf{C}} = \mathbf{C}_1 \text{ (in-plane)} + \mathbf{C}_2 \text{ (shear behaviour)} + \mathbf{C}_3 \text{ (normal)} \tag{5b}$$

where this components can be defined as:

$$\begin{cases} \mathbf{C}_1 = C_{11}\mathbf{t}^1 \otimes \mathbf{t}^1 + C_{22}\mathbf{t}^2 \otimes \mathbf{t}^2 + C_{12}(\mathbf{t}^1 \otimes \mathbf{t}^2 + \mathbf{t}^2 \otimes \mathbf{t}^1) \\ \mathbf{C}_2 = C_{13}(\mathbf{t}^1 \otimes \mathbf{t}^3 + \mathbf{t}^3 \otimes \mathbf{t}^1) + C_{23}(\mathbf{t}^2 \otimes \mathbf{t}^3 + \mathbf{t}^3 \otimes \mathbf{t}^2) \\ \mathbf{C}_2 = C_{33}\mathbf{t}^3 \otimes \mathbf{t}^3 \end{cases} \tag{5c}$$
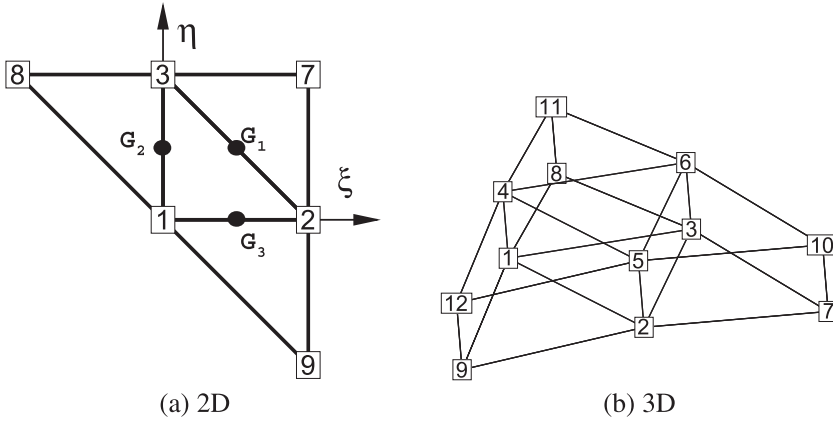
(a) 2D   (b) 3D

Figure 1. Patch performed in the element considering the neighbour elements.

Table 1. Derivatives of the shape functions from (6).

	1	2	3	7	8	9
N^I_ξ	$-1 + \eta$	$1 - \eta$	$z - \xi$	$\frac{1}{2} - z$	$\xi - \frac{1}{2}$	0
N^I_η	$-1 + \xi$	$z - \eta$	$1 - \xi$	$\frac{1}{2} - z$	0	$\eta - \frac{1}{2}$

2.2.1. In-plane behaviour

The improvement in the in-plane behaviour is the same considered for the **EBST** (Flores and Oñate, 2011, 2005; Oñate & Flores, 2005) element, a rotation-free shell element, where a four-element patch is considered (Figure 1), and the neighbour nodes allows us to work with a quadratic element in the in-plane behaviour; for more information about this element we address the reader to Oñate and Flores (2005), Flores and Oñate (2005). The same computations from the **EBST** element can be considered in the upper and lower face as we can see in the quadratic shape functions from (6) and it derivatives in Table 1.

$$N^1 = (z + \xi\eta), N^7 = \frac{z}{2}(z - 1),$$
$$N^2 = (\xi + \eta z), N^8 = \frac{\xi}{2}(\xi - 1),$$
$$N^3 = (\eta + z\xi), N^9 = \frac{\eta}{2}(\eta - 1) \tag{6}$$

We define a local system of coordinates from (3b) taking as reference the components $\mathbf{f}_1$ and $\mathbf{f}_2$ in the tangent plane and $\mathbf{f}_3$ in the normal. In each mid-side point of the element we compute the in-plane Jacobian as shown in (7a).

$$\mathbf{J} = \begin{bmatrix} \mathbf{X}_\xi \cdot \mathbf{t}_1 & \mathbf{X}_\eta \cdot \mathbf{t}_1 \\ \mathbf{X}_\xi \cdot \mathbf{t}_2 & \mathbf{X}_\eta \cdot \mathbf{t}_2 \end{bmatrix} \tag{7a}$$

And in combination of the shape function derivatives we can compute the *Cartesian* derivatives in (7b).

$$\begin{bmatrix} N_1^I \\ N_2^I \end{bmatrix}^K = \mathbf{J}_K^{-1} \begin{bmatrix} N_\xi^I \\ N_\eta^I \end{bmatrix}^K \tag{7b}$$

With the *Cartesian* derivatives we can calculate the in-plane deformation gradient components $\mathbf{f}_1^K$ and $\mathbf{f}_2^K$, and with it C_{ij}^K which are averaged over each integration point along the thickness with (8a). As with the rotation-free shells, when a neighbour is missing the values from the central node of the face are used for the averaging.

$$\bar{C}_{ij}(\xi) = L^1 \bar{C}_{ij}^1 + L^2 \bar{C}_{ij}^2 \tag{8a}$$

The variations are computed as (8b).

$$\delta \begin{bmatrix} \frac{1}{2}\bar{C}_{11} \\ \frac{1}{2}\bar{C}_{22} \\ \bar{C}_{12} \end{bmatrix} = \delta \begin{bmatrix} \frac{1}{2}\bar{C}_{11}^1 \\ \frac{1}{2}\bar{C}_{22}^1 \\ \bar{C}_{12}^1 \end{bmatrix} L^1 + \delta \begin{bmatrix} \frac{1}{2}\bar{C}_{11}^2 \\ \frac{1}{2}\bar{C}_{22}^2 \\ \bar{C}_{12}^2 \end{bmatrix} L^2 = \delta \begin{bmatrix} \bar{E}_{11} \\ \bar{E}_{22} \\ 2\bar{E}_{12} \end{bmatrix} \tag{8b}$$

At each face a modified tangent matrix $\bar{\mathbf{B}}^f$ relating the incremental tensor components with the incremental displacements $\delta \mathbf{u}$ can be written as shown in (9), where just the nodes from the face and it opposite neighbour is considered.

$$\left(\bar{\mathbf{B}}_m^f \right)_{3x18} \delta \mathbf{u}^f = \delta \begin{bmatrix} \frac{1}{2}\bar{C}_{11}^f \\ \frac{1}{2}\bar{C}_{22}^f \\ \bar{C}_{12}^f \end{bmatrix} = \frac{1}{3}\sum_{K=1}^{3} \delta \begin{bmatrix} \frac{1}{2}\bar{C}_{11}^K \\ \frac{1}{2}\bar{C}_{22}^K \\ \bar{C}_{12}^K \end{bmatrix}$$

$$= \frac{1}{3}\sum_{K=1}^{3}\sum_{J=1}^{4} \begin{bmatrix} \mathbf{f}_1^K N_1^{J(K)} \\ \mathbf{f}_2^K N_2^{J(K)} \\ (\mathbf{f}_1^K N_2^{J(K)} + \mathbf{f}_2^K N_1^{J(K)}) \end{bmatrix} \delta \mathbf{u}^{J(K)} \tag{9}$$

Once the upper and lower in-plane deformation matrices have been computed we can obtain the deformation matrix corresponding to the integration point by interpolating (10).

$$[\bar{\mathbf{B}}_m]_{3x36} = \begin{bmatrix} L^1 \bar{\mathbf{B}}_m^1 & L^2 \bar{\mathbf{B}}_m^2 \end{bmatrix} \tag{10}$$

We can obtain the equivalent nodal force vector from the integral (11), with $\int_{-1}^1 S_{ij} L^f J d\xi = \bar{S}_{ij}^f$.

$$\mathbf{r}_m^T \delta \mathbf{u} = \int_{-1}^{1} \begin{bmatrix} S_{11} \\ S_{22} \\ S_{12} \end{bmatrix}^T \begin{bmatrix} L^1 \bar{\mathbf{B}}_m^1 & L^2 \bar{\mathbf{B}}_m^2 \end{bmatrix} J d\xi$$

$$= \left\{ \begin{bmatrix} \bar{S}_{11}^1 \\ \bar{S}_{22}^1 \\ \bar{S}_{12}^1 \end{bmatrix}^T \bar{\mathbf{B}}_m^1, \begin{bmatrix} \bar{S}_{11}^2 \\ \bar{S}_{22}^2 \\ \bar{S}_{12}^2 \end{bmatrix}^T \bar{\mathbf{B}}_m^2 \right\} \delta \mathbf{u} \tag{11}$$

In (12) the calculation of geometric stiffness for the membrane behaviour is presented, where we sum the contribution of the n_G integrations points along the direction ζ.

$$
\delta\mathbf{u}^T\mathbf{K}_{mG}\Delta\mathbf{u} = \int_V \frac{\partial}{\partial\mathbf{u}}\left(\delta\begin{bmatrix}\frac{1}{2}\bar{C}_{11}\\\frac{1}{2}\bar{C}_{22}\\\bar{C}_{12}\end{bmatrix}\right)^T\begin{bmatrix}S_{11}\\S_{22}\\S_{12}\end{bmatrix}\Delta\mathbf{u}dv
$$

$$
= \sum_{G=1}^{n_G}\frac{Vol_G}{3}\sum_{f=1}^{2}L^f\sum_{K=1}^{3}\sum_{J=1}^{4}\left\{\delta\mathbf{u}^I\begin{bmatrix}N_1^I & N_2^I\end{bmatrix}\begin{bmatrix}S_{11} & S_{12}\\S_{21} & S_{22}\end{bmatrix}\begin{bmatrix}N_1^I\\N_2^I\end{bmatrix}\right\}^K
$$

(12a)

In (12b) the expression is simplified considering the already integrated stresses from (11).

$$
\delta\mathbf{u}^T\mathbf{K}_{mG}\Delta\mathbf{u} \rightarrow \text{ Considering } \int_{-1}^{1}S_{ij}L^fJd\xi = \bar{S}_{ij}^f
$$

$$
= \sum_{f=1}^{2}\sum_{K=1}^{3}\sum_{J=1}^{4}\left\{\delta\mathbf{u}^I\begin{bmatrix}N_1^I & N_2^I\end{bmatrix}^K\left[\sum_{G=1}^{n_G}\frac{V_G}{3}L^f\begin{bmatrix}\bar{S}_{11} & \bar{S}_{12}\\\bar{S}_{21} & \bar{S}_{22}\end{bmatrix}\right]\begin{bmatrix}N_1^I\\N_2^I\end{bmatrix}^K\Delta\mathbf{u}^J\right\}
$$

(12b)

$$
= \sum_{f=1}^{2}\left\{\sum_{K=1}^{3}\sum_{J=1}^{4}\left\{\delta\mathbf{u}^I\begin{bmatrix}N_1^I & N_2^I\end{bmatrix}^K\begin{bmatrix}\bar{S}_{11}^f & \bar{S}_{12}^f\\\bar{S}_{21}^f & \bar{S}_{22}^f\end{bmatrix}\begin{bmatrix}N_1^I\\N_2^I\end{bmatrix}^K\Delta\mathbf{u}^J\right\}\right\}^f
$$

2.2.2. Transverse shear behaviour

To avoid the transverse shear locking, we introduce an interpolation in natural coordinates of mixed tensorial components, a very common practice in the literature. We consider a linear variation of the transverse shear strain tangent to the side. Here, we compute a mixed components of the right *Cauchy-Green* tensor as (13), where the components relatives to the transverse shear $C_{\eta 3}$ and $C_{\xi 3}$ are written with respect to a mixed coordinate system that includes the in-plane natural coordinates (η, ξ) and the spatial local coordinate in the transverse direction (y_3). The components are written in terms of the transverse shear strain tangent to the side computed in each mid-side point, as seen in Figure 2. Besides that, the numerical integration is performed along the axis, which means $\mathbf{P}(\frac{1}{3}, \frac{1}{3})$.

$$
\begin{bmatrix}C_{\xi 3}\\C_{\eta 3}\end{bmatrix} = \begin{bmatrix}-\eta & -\eta & 1-\eta\\\xi & \xi-1 & \xi\end{bmatrix}\begin{bmatrix}\sqrt{2}C_{t3}^1\\-C_{\eta 3}^2\\C_{\xi 3}^3\end{bmatrix} = \mathbf{P}(\xi, \eta)\begin{bmatrix}\sqrt{2}\mathbf{f}_t^1\cdot\mathbf{f}_3^1\\-\mathbf{f}_\eta^2\cdot\mathbf{f}_3^2\\\mathbf{f}_\eta^3\cdot\mathbf{f}_3^3\end{bmatrix}
$$

(13)

The deformation gradient components are $\mathbf{f}_t$ (natural coordinate derivative) and $\mathbf{f}_3$ (local Cartesian coordinate derivative), these are expressed in (14a), where $\mathbf{j}_3^{-T}$ are third column of the inverse of the transverse of the Jacobian.
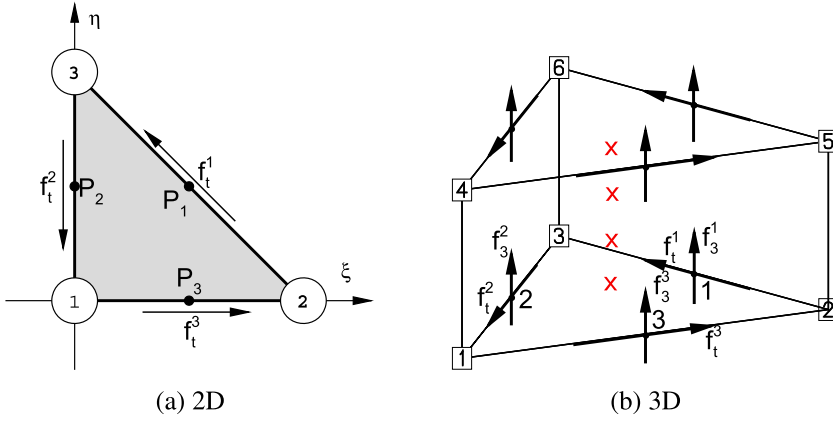
(a) 2D　　　　　　　　　　(b) 3D

Figure 2. Nodes considered in the computation of the transverse shear strains.

$$\begin{bmatrix} \bar{C}_{12} \\ \bar{C}_{23} \end{bmatrix} = \mathbf{J}_p^{-1} \begin{bmatrix} C_{\xi 3} \\ C_{\eta 3} \end{bmatrix} = \mathbf{J}_p^{-1} \mathbf{P}_a \begin{bmatrix} \mathbf{f}_t^1 \cdot \mathbf{f}_3^1 \\ -\mathbf{f}_\eta^2 \cdot \mathbf{f}_3^2 \\ \mathbf{f}_\xi^3 \cdot \mathbf{f}_3^3 \end{bmatrix} \tag{14a}$$

$$\mathbf{f}_3 = \sum_{I=1}^{6} N_3^I \mathbf{x}^I = \begin{bmatrix} \mathbf{f}_\xi & \mathbf{f}_\eta & \mathbf{f}_\zeta \end{bmatrix} \begin{bmatrix} \frac{\partial \xi}{\partial y_3} \\ \frac{\partial \eta}{\partial y_3} \\ \frac{\partial \eta}{\partial y_3} \end{bmatrix} = \nabla_\xi (\mathbf{x}) \mathbf{j}_3^{-T} \tag{14b}$$

The modified transverse shear Cartesian components can be obtained from (14c), interpolating these values the components from the right *Cauchy-Green* tensor can be obtained (14d).

$$\begin{bmatrix} \sqrt{2} \mathbf{f}_t^1 \\ -\mathbf{f}_\eta^2 \\ \mathbf{f}_\xi^3 \end{bmatrix}^1 = \begin{bmatrix} \mathbf{x}^3 - \mathbf{x}^2 \\ \mathbf{x}^1 - \mathbf{x}^3 \\ \mathbf{x}^2 - \mathbf{x}^1 \end{bmatrix}, \quad \begin{bmatrix} \sqrt{2} \mathbf{f}_t^1 \\ -\mathbf{f}_\eta^2 \\ \mathbf{f}_\xi^3 \end{bmatrix}^2 = \begin{bmatrix} \mathbf{x}^6 - \mathbf{x}^5 \\ \mathbf{x}^4 - \mathbf{x}^6 \\ \mathbf{x}^5 - \mathbf{x}^4 \end{bmatrix} \tag{14c}$$

$$\begin{bmatrix} \bar{C}_{13} \\ \bar{C}_{23} \end{bmatrix} (\zeta) = \begin{bmatrix} \bar{C}_{12} \\ \bar{C}_{23} \end{bmatrix}^1 L^1 + \begin{bmatrix} \bar{C}_{13} \\ \bar{C}_{23} \end{bmatrix}^2 L^2 = \begin{bmatrix} 2E_{13} \\ 2E_{23} \end{bmatrix} (\zeta) \tag{14d}$$

The tangent matrix $\bar{\mathbf{B}}_s$ is also obtained by interpolating from both faces (15a). In a similar way to the in-plane behaviour, the internal forces can be obtained from (15c). Finally, the geometric stiffness matrix can be obtained from (15e).

$$\bar{\mathbf{B}}_s(\zeta) = \bar{\mathbf{B}}_s^1 L^1 + \bar{\mathbf{B}}_s^2 L^2 \tag{15a}$$

where $\bar{\mathbf{B}}_s^f$ is defined the following way:

$$\bar{\mathbf{B}}_s^f = \left(\mathbf{J}_p^f \right)^{-1} \mathbf{P}_a \tilde{\mathbf{B}}_s^f \quad \text{and} \quad \tilde{\mathbf{B}}_s \delta \mathbf{u}^e = \begin{bmatrix} \delta \mathbf{f}_t^1 \cdot \mathbf{f}_3^1 + \mathbf{f}_t^1 \cdot \delta \mathbf{f}_3^1 \\ -\delta \mathbf{f}_\eta^2 \cdot \mathbf{f}_3^2 - \mathbf{f}_\eta^2 \cdot \delta \mathbf{f}_3^2 \\ \delta \mathbf{f}_\xi^3 \cdot \mathbf{f}_3^3 + \mathbf{f}_\xi^3 \cdot \delta \mathbf{f}_3^3 \end{bmatrix} \tag{15b}$$

$$\mathbf{r}_s^T = \int_V \begin{bmatrix} \bar{S}_{12} \\ \bar{S}_{23} \end{bmatrix} [\bar{\mathbf{B}}_s]_{2x18} \, \mathrm{d}v = \bar{\mathbf{Q}}_{4x1}^T \begin{bmatrix} \bar{\mathbf{B}}_s^1 \\ \bar{\mathbf{B}}_s^2 \end{bmatrix}_{4x18} \tag{15c}$$

where $\bar{\mathbf{Q}}_{4x1}^T$ corresponds with the shear internal forces and can be defined as:

$$\bar{\mathbf{Q}}_{4x1}^T = \int_{-1}^{1} \begin{bmatrix} \begin{bmatrix} \bar{S}_{12} \\ \bar{S}_{23} \end{bmatrix} L^1 \\ \begin{bmatrix} \bar{S}_{12} \\ \bar{S}_{23} \end{bmatrix} L^2 \end{bmatrix} J d\zeta \tag{15d}$$

$$\delta \mathbf{u}^T \mathbf{K}_{sG} \Delta \mathbf{u} = \Delta \left\{ \begin{bmatrix} \bar{\mathbf{B}}^1 \\ \mathbf{B}_s^2 \end{bmatrix} \delta \mathbf{u} \right\}^T \bar{\mathbf{Q}} \rightarrow [\bar{Q}_1 \ \bar{Q}_2] \Delta \left(\bar{B}_s^1 \delta \mathbf{u} \right)$$

$$= \frac{1}{3} \begin{pmatrix} \left(-\bar{Q}_1' + \bar{Q}_2' \right) \left(\sqrt{2} \delta \mathbf{f}_t^1 \cdot \Delta \mathbf{f}_3^1 + \sqrt{2} \Delta \mathbf{f}_t^1 \cdot \delta \mathbf{f}_3^1 \right) \\ \left(-\bar{Q}_1' - 2\bar{Q}_2' \right) \left(-\delta \mathbf{f}_\eta^2 \cdot \Delta \mathbf{f}_3^2 + \Delta \mathbf{f}_t^2 \cdot \delta \mathbf{f}_3^2 \right) \\ \left(2\bar{Q}_1' + \bar{Q}_2' \right) \left(\delta \mathbf{f}_\xi^3 \cdot \Delta \mathbf{f}_3^3 + \Delta \mathbf{f}_\xi^3 \cdot \delta \mathbf{f}_3^3 \right) \end{pmatrix} \tag{15e}$$

With $\left[\bar{Q}_1' \ \bar{Q}_2' \right] = [\bar{Q}_1 \ \bar{Q}_2] J_p^{-1}$

2.2.3. Transverse normal behaviour

As introduced previously, to avoid locking (volumetric locking) in quasi-incompressible problems due to the *Poisson* effect the **EAS** (Enhanced Assumed Strain) formulation is considered. With this formulation we obtain a modified $\mathbf{C}_3$ component.

2.2.3.1. EAS formulation.
In the standard **EAS** method, the convective strain components are interpolated, in our case as we just want to improve $\mathbf{C}_3$ and some modifications as presented below are considered. At the element centre ($\xi = \eta = \frac{1}{3}$ and $\zeta = 0$) the *Cartesian* deformation gradient, and in consequence the right *Cauchy* tensor, can be enhanced as shown in (16). So, in this **EAS** the changes will affect just to the C_{33} component, and the C_{13} and C_{23} are computed as presented in the previous section.

$$\mathbf{f}_3^C = \sum_{I=1}^{6} N_3^{IC} \mathbf{X}^I \rightarrow \bar{\mathbf{f}}_3 = \mathbf{f}_3^C e^{\alpha \zeta} \rightarrow \bar{C}_{33} = \bar{\mathbf{f}}_3 \cdot \bar{\mathbf{f}}_3 = C_{33}^2 e^{2\alpha \zeta} \tag{16}$$

With this enhancement the deformation matrix, internal forces and geometric stiffness can be calculated as shown in (17).

$$\delta \bar{E}_{33} = \frac{1}{2} \delta \bar{C}_{33} = \delta \mathbf{f}_3^C \cdot \mathbf{f}_3^C e^{2\alpha \zeta} + \bar{C}_{33} \zeta \delta \alpha$$

$$= \left(\sum_{I=1}^{6} N_3^{IC} \delta \mathbf{u}^I \right) \cdot \mathbf{f}_3^C e^{2\alpha \zeta} + \bar{C}_{33} \zeta \delta \alpha = e^{2\alpha \zeta} \mathbf{B}_3^C \delta \mathbf{u}^e + \bar{C}_{33} \zeta \delta \alpha \tag{17a}$$

$$\mathbf{r}_n^T = \int_V \mathbf{B}_3 S_{33} \mathrm{d}v = \int_{-1}^{1} e^{2\alpha\zeta} \mathbf{B}_3^C S_{33} J d\zeta = \mathbf{B}_3^C \bar{S}_{33} \qquad (17b)$$

With the normal enhanced stress $\bar{S}_{33} = \int_{-1}^{1} e^{2\alpha\zeta} S_{33} J d\zeta$.

$$\delta\mathbf{u}^T \mathbf{K}_{Gn} \Delta\mathbf{u} = \delta\mathbf{f}_3^C \cdot \Delta\mathbf{f}_3^C \bar{S}_{33} = \sum_{I=1}^{6} (\delta\mathbf{u}^I)^T \sum_{J=1}^{6} N_3^{IC} N_3^{JC} \bar{S}_{33} \mathbf{A} \Delta\mathbf{u}^J \qquad (17c)$$

where the assembling matrix $\mathbf{A} = \begin{bmatrix} 1 & & \\ & 1 & \\ & & 1 \end{bmatrix}$

2.2.3.2. Balance equation. In the following lines we will introduce the balance equation which allows us to obtain the implicit solution of the problem. Because we will focus in the implicit solution of the problem we will address the reader to Flores (2013a, 2013b, 2013c) where the explicit solution of the problem is presented too.

The balance equation related with α **DOF** from (4) can be expressed as (18a), where we can obtain the residue and approximating the solution with a *Newton-Raphson* technique the residual can be nullified (18b).

$$\delta\alpha \int_{-1}^{1} S_{33} \bar{C}_{33} \zeta J d\zeta = 0 \rightarrow r_\alpha = \int_{-1}^{1} S_{33} \bar{C}_{33} \zeta J d\zeta \qquad (18a)$$

$$\int_{-1}^{1} \left[\frac{\partial S_{33} \bar{C}_{33}}{\partial \mathbf{u}} \Delta\mathbf{u} + \frac{\partial S_{33} \bar{C}_{33}}{\partial \alpha} \Delta\alpha \right] \zeta J d\zeta + r_\alpha = 0 \qquad (18b)$$

With the derivatives $\frac{\partial S_{33} \bar{C}_{33}}{\partial \mathbf{u}}$ and $\frac{\partial S_{33} \bar{C}_{33}}{\partial \alpha}$ being defined as:

$$\begin{cases} \frac{\partial S_{33} \bar{C}_{33}}{\partial \mathbf{u}} = \bar{C}_{33} \mathbf{D}_3 \bar{\mathbf{B}} + 2 S_{33} \bar{\mathbf{B}}_3 \\ \frac{\partial S_{33} \bar{C}_{33}}{\partial \alpha} = \bar{C}_{33} \left(D_{33} \bar{C}_{33} \zeta + 2 S_{33} \zeta \right) \end{cases} \qquad (18c)$$

Substituting (18c) into (18b) the expression (19a), from which we can deduce the $\Delta\alpha$ necessary to obtain the equilibrium.

$$\int_{-1}^{1} \left[\left(\bar{C}_{33} \mathbf{D}_3 \bar{\mathbf{B}} + 2 S_{33} \bar{\mathbf{B}}_3 \right) \Delta\mathbf{u} + \bar{C}_{33} \left(D_{33} \bar{C}_{33} \zeta + 2 S_{33} \zeta \right) \Delta\alpha \Delta\alpha \right] \zeta J d\zeta + r_\alpha = 0 \qquad (19a)$$

The previous expression can be condensed in the following expression(19b), where after integrate the operators $\mathbf{H}$ and k_α are obtained (19c).

$$\mathbf{H}_{1x18} \Delta\mathbf{u} + k_\alpha \Delta\alpha + r_\alpha = 0 \text{ then } \Delta\alpha = \frac{r_\alpha}{k_\alpha} - \frac{1}{k_\alpha} \mathbf{H} \Delta\mathbf{u} \qquad (19b)$$

The full definition of $\mathbf{H}_{1x18}$ and k_α is detailed below:

$$\begin{cases} \mathbf{H} = \int_{-1}^{1} \left(\bar{C}_{33}\mathbf{D}_3\bar{\mathbf{B}} + 2S_{33}\bar{\mathbf{B}} \right) \zeta J \mathrm{d}\zeta \\ k_\alpha = \int_{-1}^{1} \bar{C}_{33} \left(D_{33}\bar{C}_{33} + 2S_{33} \right) \zeta^2 J \mathrm{d}\zeta \end{cases} \tag{19c}$$

If the expression is introduced in the balance equation associated with the displacement in (4) we can obtain (20a).

$$\delta\mathbf{u}^T \int_V \bar{\mathbf{B}}^T \mathbf{S} \mathrm{d}v - \delta\mathbf{u}^T G_{ext} = \delta\mathbf{u}^T \mathbf{r}(\mathbf{u},\alpha) \tag{20a}$$

From the balance equation the usual finite element matrix system can be obtained, first (20a) can be linearised in the expression (20b).

$$\int_{-1}^{1} \left[\bar{\mathbf{B}}^T \left(\frac{\partial \mathbf{S}}{\partial \mathbf{u}}\Delta\mathbf{u} + \frac{\partial \mathbf{S}}{\partial \alpha}\Delta\alpha \right) + \left(\frac{\partial \bar{\mathbf{B}}^T}{\partial \mathbf{u}}\Delta\mathbf{u} + \frac{\partial \bar{\mathbf{B}}^T}{\partial \alpha}\Delta\alpha \right) \mathbf{S} \right] J \mathrm{d}\zeta + \mathbf{r}(\mathbf{u}) = \mathbf{0} \tag{20b}$$

Substituting in (20b) with the standard finite element expressions and (18c).

$$\int_{-1}^{1} \left[\bar{\mathbf{B}}^T \left(\mathbf{D}\bar{\mathbf{B}}\Delta\mathbf{u} + \mathbf{D}_3^T\bar{C}_{33}\zeta\Delta\alpha \right) + \mathbf{S}\mathbf{G}\Delta\mathbf{u} + 2S_{33}\bar{\mathbf{B}}_3^T\zeta\Delta\alpha \right] J \mathrm{d}\zeta + \mathbf{r}(\mathbf{u}) = \mathbf{0} \tag{20c}$$

Reordering (20c) we can obtain (20d).

$$\int_{-1}^{1} \left[\left(\mathbf{B}^T\mathbf{D}\bar{\mathbf{B}}\mathbf{S}\mathbf{G} \right)\Delta\mathbf{u} + \left(\bar{\mathbf{B}}^T\mathbf{D}_3^T\bar{C}_{33} + 2S_{33}\bar{\mathbf{B}}_3^T \right)\zeta\Delta\alpha \right] J \mathrm{d}\zeta + \mathbf{r}(\mathbf{u}) = \mathbf{0} \tag{20d}$$

The system can be expressed as a fully integrated matrix system (20e), where $\mathbf{K_T} = \mathbf{K_M} + \mathbf{K_G} = \int_{-1}^{1} \bar{\mathbf{B}}^T\mathbf{D}\bar{\mathbf{B}}J\mathrm{d}\zeta + \int_{-1}^{1} \mathbf{S}\mathbf{G}J\mathrm{d}\zeta$.

$$\left(\mathbf{K}_T\Delta\mathbf{u} + \mathbf{H}^T\Delta\alpha \right) + \mathbf{r}(\mathbf{u}) = \mathbf{0} \tag{20e}$$

Substituting in the last expression with (19b).

$$\mathbf{K}_T\Delta\mathbf{u} - \mathbf{H}^T \left(\frac{r_\alpha}{k_\alpha} + \frac{1}{k_\alpha}\mathbf{H}\Delta\mathbf{u} \right) + \mathbf{r}(\mathbf{u}) = \mathbf{0} \tag{20f}$$

Finally all this can be expressed (20g) as a modification of the elemental tangent stiffness matrix and the internal forces.

$$\left(\mathbf{K}_T - \mathbf{H}^T\frac{1}{k\alpha}\mathbf{H} \right)\Delta\mathbf{u} - \mathbf{H}^T\frac{r_\alpha}{k_\alpha} + \mathbf{r}(\mathbf{u}) = \mathbf{0} \tag{20g}$$

Reordering (20g), (20h) can be obtained.

$$\begin{cases} \bar{\mathbf{K}}_T = \mathbf{K}_T - \mathbf{H}^T\frac{1}{k_\alpha}\mathbf{H} \\ \bar{\mathbf{r}} = \mathbf{r} - \mathbf{H}^T\frac{r_\alpha}{k_\alpha} \end{cases} \tag{20h}$$

2.2.3.3. Pull-Back and Push-Forward (Extension of the formulation). The formulation presented until now is broadly the formulation already presented in the works of Flores (2013a, 2013b, 2013c), the main step forward of this work is the extension of the formulation. As we have seen the formulation presented allows us to obtain a modified left *Cauchy* tensor $\bar{\mathbf{C}}$. With this tensor we are able to obtain strains in a traditional way, *g.e* with *Green-Lagrange*, but we are unable to work with the **Pull-Back** and **Push-Forward** operations, these are furthermore the underlying operations in the constitutive operations in *Kratos*. The fundamental concepts for this are presented in the Appendix 1.

In order to perform these operations we need the deformation gradient $\mathbf{F}$, or in our case $\bar{\mathbf{F}}$ owing to we are working with a modified right *Cauchy* tensor $\bar{\mathbf{C}}$. Obtain one from another is not a trivial operation, and we must consider additional assumptions to obtain our modified deformation gradient. In a standard formulation to obtain the deformation gradient $\mathbf{F}$ we compute (21) from the material displacement gradient tensor $\nabla_{\mathbf{X}}\mathbf{u}$, $\mathbf{C}$ can be obtained easily from here.

$$\mathbf{F} = \nabla_{\mathbf{X}}\mathbf{u} + \mathbf{I} \rightarrow \mathbf{C} = \mathbf{F}^T\mathbf{F} \tag{21}$$

We will present now (22a) the polar decomposition of $\mathbf{F}$, which will be the key idea considered to obtain $\bar{\mathbf{F}}$. In this decomposition $\mathbf{R}$ represents the *proper orthogonal tensor* and $\mathbf{U}$ is the *right stretch tensor*. The *right stretch tensor* can be computed from the square root of the right *Cauchy* tensor (22b). The only remaining component needed to compute the $\bar{\mathbf{F}}$ will be the modified *proper orthogonal tensor* where we will take the assumption of $\bar{\mathbf{R}} = \mathbf{R}$. The computation of this $\bar{\mathbf{F}}$ is summarized in (22c).

$$\mathbf{F} = \mathbf{R}\mathbf{U} \text{ thus } \bar{\mathbf{F}} = \bar{\mathbf{R}}\bar{\mathbf{U}} \tag{22a}$$

$$\mathbf{U} = \sqrt{\mathbf{C}} \text{ thus } \bar{\mathbf{U}} = \sqrt{\bar{\mathbf{C}}} \tag{22b}$$

$$\bar{\mathbf{F}} = \mathbf{R}\bar{\mathbf{U}} \begin{cases} \mathbf{C} = \mathbf{F}^T\mathbf{F} \rightarrow \mathbf{U} = \sqrt{\mathbf{C}} \rightarrow \mathbf{R} = \mathbf{F} \cdot \mathbf{U}^{-1} \\ \bar{\mathbf{U}} = \sqrt{\bar{\mathbf{C}}} \end{cases} \tag{22c}$$

3. Test cases

First of all, we consider as reference the results obtained with previous implementations of the element by Flores (2013a, 2013b), as well as the results from Sze, Liu, and Lo (2004), Klinkel et al. (2006). In the following, when '**Ref.**' is displayed will refer to this; meanwhile when '**Cal.**'[3] is displayed the simulation will have been performed with the *in-home* implementation in *Kratos*.
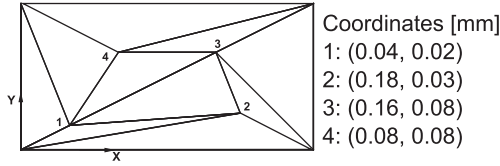
Coordinates [mm]
1: (0.04, 0.02)
2: (0.18, 0.03)
3: (0.16, 0.08)
4: (0.08, 0.08)

Figure 3. Patch test geometry.

3.1. Patch test

The first step in the implementation of an element into a **FEM** code is the verification of the kinematics, for this reason the patch test is understood as a necessary condition for the convergence of the element. In the case of solid elements it is expected that when nodal displacements corresponding to a constant strain gradient (membrane patch test) are imposed, constant efforts are obtained in all the elements; so in owing to the SPRISM is in fact a solid element this is the behaviour we should expect. In the case of a solid-shell element clearly this must satisfy at least the membrane patch test and, although it may not be necessary, it is highly desirable that the element satisfies the bending patch test as this will lead to a more robust and reliable element.

Figure 3 shows a patch of elements that has been widely used to access quadrilateral shell elements and hexahedral solid shell elements, like where are working with prisms (wedges), we should split in two these elements. The size of the largest sides is $a = 0.24$ mm and the size of the shortest side is $b = 0.12$ mm, while the thickness considered is $t = 0.001$ mm. The lower surface has been located at coordinate $z = -t/2$. The mechanical properties of the material are: *Young's* modulus $E = 10^6$ MPa and Poisson ratio $v = 0.25$. Because the problem considered is linear just 2 integration points across the thickness are used located in the usual Gauss quadrature positions ($\zeta = \pm 1/\sqrt{3}$).

3.2. Membrane patch test

The prescribed nodal displacements (on the boundary nodes) are defined by the linear functions (23), and $u_z = 0$ only on the nodes in the lower face to allow contraction due to *Poisson* effect. Due to the pure membrane strains developed in this test, the internal **DOF** α obtained is zero and constant in all the elements.

$$\begin{cases} u_x = \left(x + \frac{y}{2}\right) \cdot 10^{-3} \\ u_y = \left(y + \frac{x}{2}\right) \cdot 10^{-3} \end{cases} \tag{23}$$

Using present element **SPRISM** the correct results are obtained for both the displacements of the interior nodes according to (23) and the element stresses ($\sigma_{xx} = \sigma_{yy} = 1333.3$ MPa and $\sigma = 400$ Mpa).
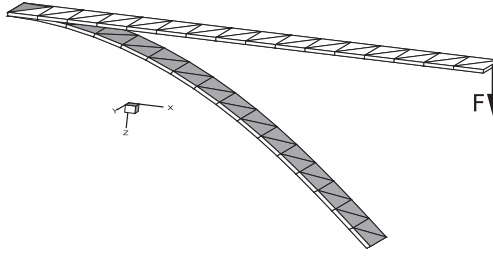
Figure 4. Cantilever with point load.

3.3. Bending patch test

In this case, the displacement field associated with a constant bending stress state is given by (24), that is prescribed on the exterior nodes of both shell faces.

$$\begin{cases} u_x = \left(x + \frac{y}{2}\right) \cdot \frac{z}{2} \cdot 10^{-3} \\ u_y = \left(y + \frac{x}{2}\right) \cdot \frac{z}{2} \cdot 10^{-3} \\ u_z = \left(x^2 + xy + y^2\right) \cdot \frac{1}{2} \cdot 10^{-3} \end{cases} \tag{24}$$

We obtain a value for the internal **DOF** α constant in all elements and equal to: $\alpha = 0.3333 \cdot 10^{-8}$. The bending stresses at the integration points are $\sigma_{xx} = \sigma_{yy} = \pm 0.3849$ Mpa,[4] and $\sigma_{xy}\pm = 0.1155$ Mpa[5] while the displacements at the interior nodes correspond exactly with expression (24). So in consequence the element satisfies this test too.

3.4. Cantilever

A cantilever plate strip of length $L = 10$ mm width $b = 1$ mm and thickness $t1 = 0.1$ mm is subjected to a transverse load $F = 40$ N (Figure 4). For the selected *Young's* modulus $E = 106$ MPa, the behaviour is one with large displacements but small strains. Using different values of *Poisson* ratio ($v = 0.0$, $v = 0.3$, $v = 0.49$, $v = 0.499$ and $v = 0.4999$ (quasi-incompresible)) it can be assessed if the proposed assumed strain techniques allow to avoid, respectively, the **transverse shear locking**, the ***Poisson* effect locking** and the **volumetric locking**. At the same time, different geometries, with different number of divisions in length have been considered (8, 16, 24, and 32 divisions), one in the width and one across the thickness with two integration points. The final deformed configurations (vertical displacement is 70% of the length) is achieved considering small load steps.

The Figure 5 shows the maximum vertical displacement vs. the load factor (from 0 to 1) for 5 different values of the *Poisson* ratio, for the geometry of the 32 divisions in length. The case $v = 0$ allows to compare with the reference value ($u_z = 7.08$ mm) and to see if the approach used to cure transverse shear locking is adequate. The result obtained $u_z = 7.06$ mm indicates that effectively
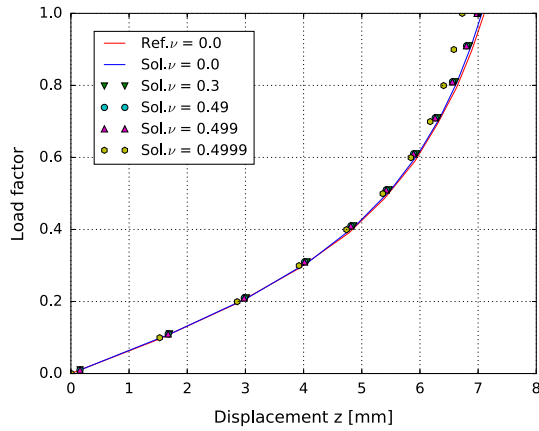
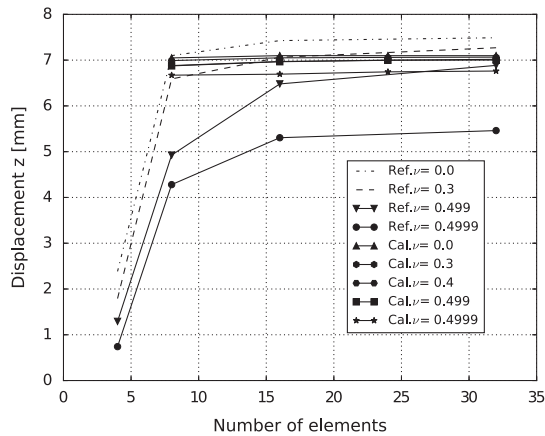**Figure 5.** Evolution of displacement with load factor.

Figure 6. Comparison of results respect ν and the number of longitudinal divisions.

the element is free of **transverse shear locking**. The second value of *Poisson* ratio ($\nu = 0.30$) is used to assess if the **EAS** technique avoids the appearance of **locking due to *Poisson's* effect**. In this case, the computed displacement is $u_z = 7.03$ mm that although is not exactly the same value obtained for $\nu = 0$ shows that the proposed method avoids the **Poisson's effect locking** allowing a proper gradation of the transverse normal strain. Finally, the last three values of *Poisson* ratio (0.49, 0.499 and 0.4999) allow to observe if the performance of the element deteriorates significantly in the quasi-incompressible range. It can be seen that although differences grow with *Poisson* ratio, this are below 4% for the higher value considered.

Besides, Figure 6 plots the tip displacement as a function of the mesh density (number of divisions along the length) for four different *Poisson's* ratio. From the reference results obtained by *Fernando G. Flores*, it can be seen that convergence
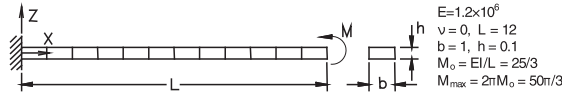
Figure 7. Cantilever subjected to end bending moment.
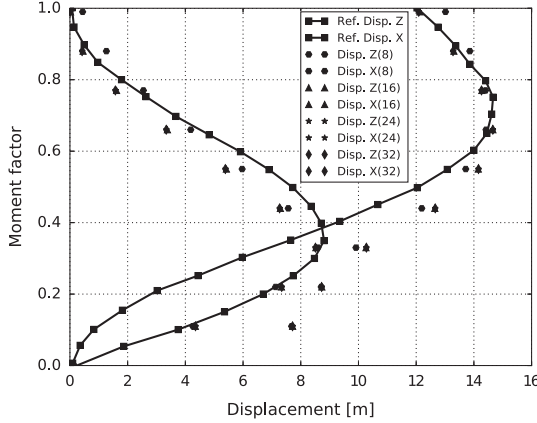
Figure 8. Solution for multiple configurations.

deteriorates for *Poisson's* ratio larger than 0.499; as it happens in our *in-home* implementation, but slightly less significant in this case.

3.5. Cantilever subjected to end bending moment

Figure 7 shows a cantilever subjected to end moment M. The problem has been considered in from the reference Sze et al. (2004). The cantilever forms a circular arc with its radius R given by the classical flexural formula $R = EI = M$. Using the formula, the analytical normalized deflections can be derived to be (25) where $M_0 = EI = L$. The maximum end moment $M_{\max}$ is taken to be M_0 at which the beam will be bent into a circle. Figure 8 plots the end moment against the vertical and horizontal tip deflections for different configurations of the geometry (8, 16 and 32 subdivisions).

$$\frac{U}{L} = \frac{M_0}{M} \sin\left(\frac{M}{M_0} - 1\right) , \frac{W}{L} = \frac{M_0}{M}\left(1 - \cos\left(\frac{M}{M_0}\right)\right) \tag{25}$$

3.6. Frequencies test

This example (extracted from Flores (2013a), Olovsson, Unosson, & Simonsson, 2004) considers the dynamic behaviour of a cantilever beam with length, width and thickness $L = 1$; $b = 0.1$ and $t = 0.01$ respectively. The mechanical properties are *Young's* modulus $E = 100\,\text{GPa}$, *Poisson's* ratio $\mu = 0$ and mass density $\rho = 1000\,\text{kg/m}^3$. The point load applied at the free side (Figure 4) has a value of $100\,\text{N}$ with a *Heaviside* step time function. As the problem is elastic with
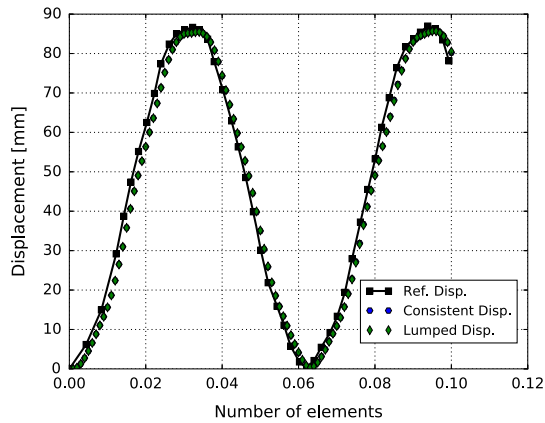
Figure 9. Frequencies behaviour test.
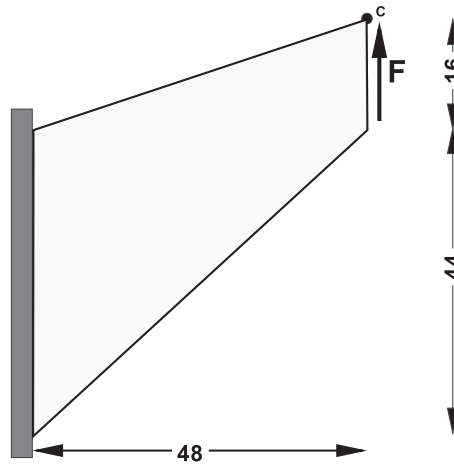
**Figure 10.** *Cook's* membrane geometry.

$\mu = 0$ there is no *Poisson*'s effect across the thickness nor volumetric locking. The behaviour is purely bending and it is useful to evaluate the shear locking and assess the proposed cure. The discretisation includes eight uniform divisions along the length, one in the width and one element through the thickness. The solution shown in Figure 9 is a very close behaviour to the reference Flores (2013a), both for lumped and consistent mass matrix.

3.7. Cook membrane

This example (see Figure 10) involves a large amount of shear energy and is commonly used to assess in-plane bending performance. Plane strain condition will be considered here with two different material behavior: (a) a quasi-incompressible elastic material with $G = 80.1938$ GPa and $K = 40.1 \cdot 10^4$ GPa corresponding with a *Poisson* ratio $\mu = 0.4999$ and (b) an elastic-plastic material

Table 2. Isotropic-kinematic hardening law constans.

Yiled stress σ_y	0.45 GPa
Kinematic hardening modulus h	0.12924 GPa
Reference hardening modulus σ_0	0.45 GPa
Infinity hardening modulus σ_∞	0.715 GPa
Hardeningexponent η	16.93
Pure isotropic hardening θ	1
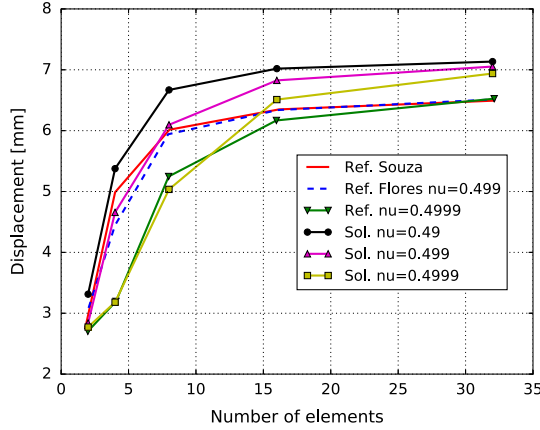
Figure 11. Displacement vs. number of elements for the elastic case.

with elastic properties $G = 80.1938$ GPa and $K = 164.21$ GPa implying a *Poisson* ratio $\mu = 0.29$ and J_2 plasticity with isotropic hardening as a function of the effective plastic strain e^p defined by (26) and the values of the Table 2.

$$\sigma_y^* = \text{Linear hardening} + \text{Exponential hardening} \qquad (26a)$$

$$\begin{cases} \text{Linear hardening} = \sigma_y + e^p \cdot \theta \cdot h \\ \text{Exponential hardening} = (\sigma_0 - \sigma_\infty) \cdot (1 - e^{-\eta \cdot e^p}) \end{cases} \qquad (26b)$$

The applied load is 100 kN for the elastic case and 5 kN for the elastic-plastic material. The plane strain condition implies coefficient $C_{33} = 1$ at all points ($\alpha = 0$), thus the version without **ANS** for the in-plane components locks due to the almost incompressibility constraint in the same way that a constant strain triangle does. Because of that this example is intended to assess how the improvement in the membrane field collaborates to cure the volumetric locking.

Figures 11 and 12 show a convergence analysis as the mesh is refined, where the vertical displacement of point **C** has been plotted vs. the number of divisions per side. The results have been compared with the reference Flores (2013b), and other results presented in the same article, where the results that we have obtained present a very good convergence in comparison.
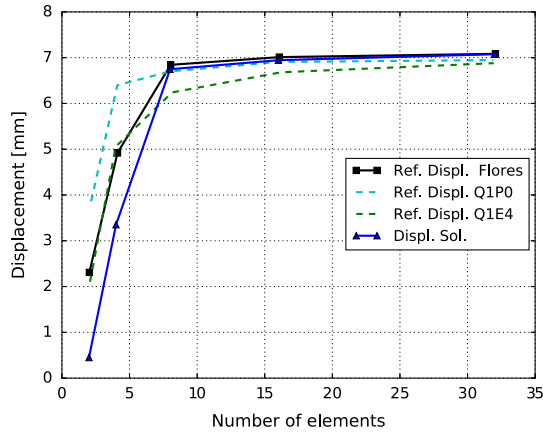
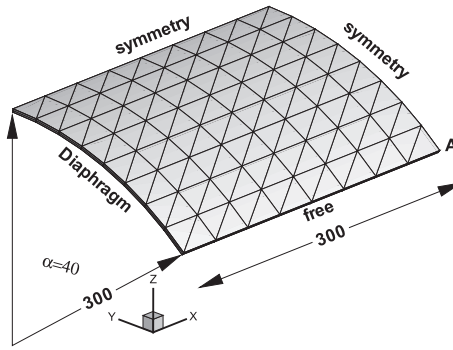**Figure 12.** Displacement vs. number of elements for the elastic-plastic case.

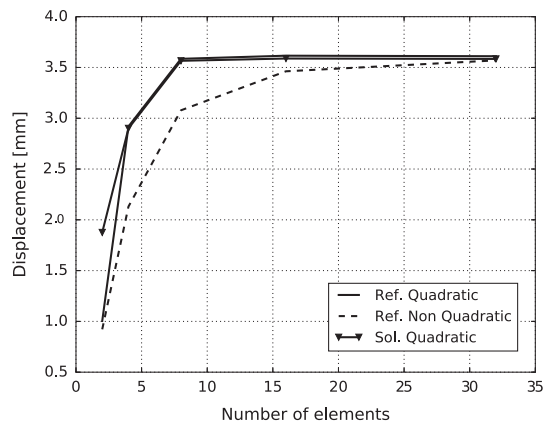**Figure 13.** Geometry of the scoordelis cylindrical roof.

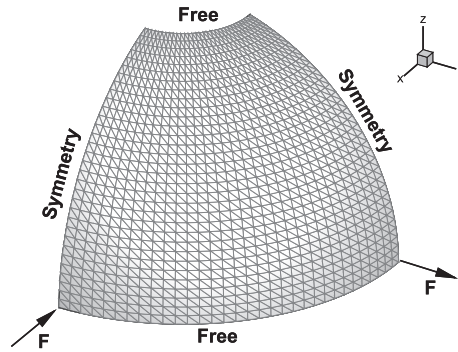**Figure 14.** Scoordelis solution. Displacement vs. number of elements.

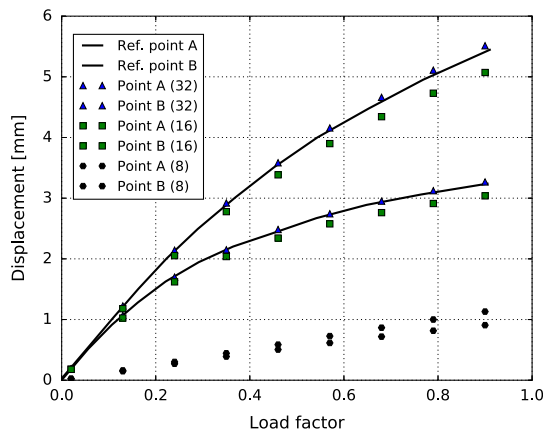**Figure 15.** Geometry of a semi-spherical shell with a hole, both original and deformed geometry.

Figure 16. Displacement vs. load for $R/t = 250$.

3.8. Scoordelis cylindrical roof test

In this example, we proceed with a linear analysis of a cylindrical shell under self weight, which is free along the one side as can be seen in the Figure 13 and it has been simplified in one quarter of the original size with additional consideration of the symmetry conditions of the problem. We have considered five different geometric configurations, with a different number of elements across the side, until the convergence of the solution have been archived. As we have mentioned previously, the problem is linear, therefore it is possible to solve the problem considering just two *Gauss* points across the thickness.

The problem is membrane dominant, that is why could be interesting to observe the relevance of the **ANS** for in-plane components in non-isochoric problems. The results obtained are shown in the Figure 14, where the results are compared with our reference Flores (2013a), having a very close convergence to the reference solution.
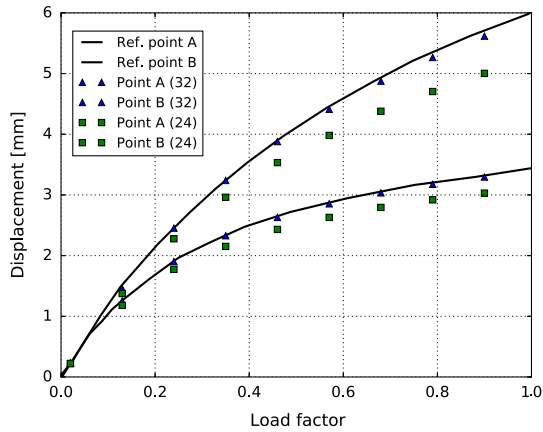
Figure 17. Displacement vs. load for $R/t = 1000$.

3.9. Sphere test

Some interesting kind of problem to check the suitability of the element is the problems where an initially double curved geometry. This problem (Figure 15) is analysed and solved recurrently in the context of large elastic displacements. The Figure 15 presents the geometry considered in the resolution of the problem, where once again the symmetry has been considered to simplify the resolution of the problem. This problem is mainly an inextensional bending problem where *Poisson* effect has an important role in the behaviour of the structure, in contrast with the membrane effect that is less significant in this problem. Additionally, the membrane locking and the curvature-thickness looking can manifest. Several meshes have been considered, with 8, 16, 24 and 32 elements by side respectively, with a middle radius of $R = 10$ mm and thickness of $t = 0.04$ mm ($R/t = 250$). The more coarsed is the element, the more it could suffer the looking effect due to the initial curvature, considering this when solution more differs more than the 5% from the target values. We are considering the following mechanical properties, $E = 6.825 \cdot 10^4$ GPa and $\nu = 0.3$ (Figures 16 and 17).

3.10. Pull-out of an open-ended cylindrical shell

Figure 18 shows an open-ended cylinder being pulled by a pair of radial forces P, this problem can be challenging owing to the fact that it involves large displacements. The problem has been considered in the Reference Sze et al. (2004), among others. Owing to symmetry, just one-eighth of the shell is modelled. As can be seen in Figure 18, the parameters considered are a *Young* modulus of $E = 10.5$ MPa, *Poisson* ratio $\nu = 0.3125$, dimensions of $R = 4.953$ m, $L = 10.35$ m, $h = 0.094$ m and maximum load of $P_{\max} = 40000$ N.

The Figure 19 presents the convergence of the solution considering a different number of elements, having a converged solution for 16 elements per side very
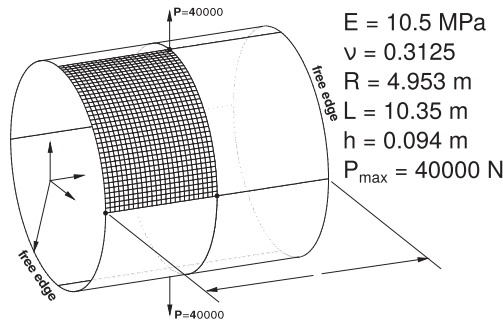
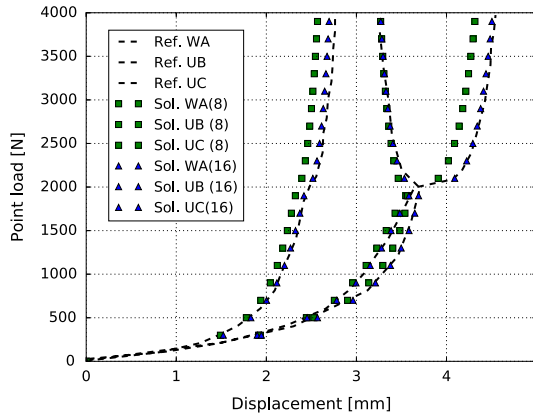**Figure 18.** The open-end cylindrical shell subjected to radial pulling forces.

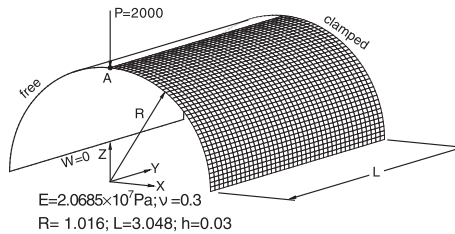**Figure 19.** Open-ended cylindrical shell problem load-deflection curves.

Figure 20. The semi-cylindrical shell subjected to an end pinching force.

close to the reference one (Sze et al., 2004), which employs a standard shell element.

3.11. Pinched semi-cylindrical

Figure 20 shows the semi-cylindrical shell (Sze et al., 2004) subjected to an end pinching force at the middle of the free-hanging circumferential periphery. The other circumferential periphery is fully clamped. Along its longitudinal edges, the vertical deflection and the rotation about the Y-axis are restrained.
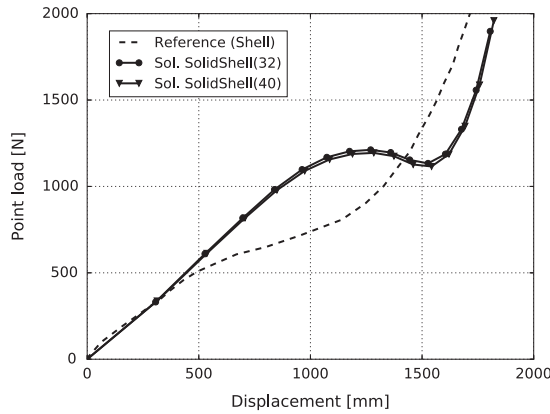
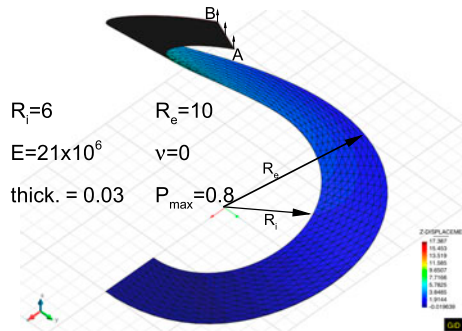**Figure 21.** Semi-cylindrical shell load-deflection curves.

Figure 22. Slit annular plate deformation solution.

The solution obtained is shown in Figure 21 presents the load-deflection curve, in our solution the behaviour obtained is slightly different from the one presented in the reference Sze et al. (2004), this can be due to the fact that we are taking the displacement in the point where the load is applied, meanwhile the reference solutions corresponds to a shell and the solution corresponds with the displacement in the middle surface; thus to improve our solution a possible way to tackle this problematic is add an additional layer and plot the solution in the point belonging to the middle surface.

3.12. Slit test

The present problem consists in an annular plate which presents a large displacement due to a load applied in one face while the other face is constrained. This problem is a common *benchmark* considered to study the behaviour of shells under large rotations, in or case owing to we are considering a **solid-shell** we do not have rotations in our element and it could be considered as large displacement problem. The solution looks like the solution expected Figure 22.
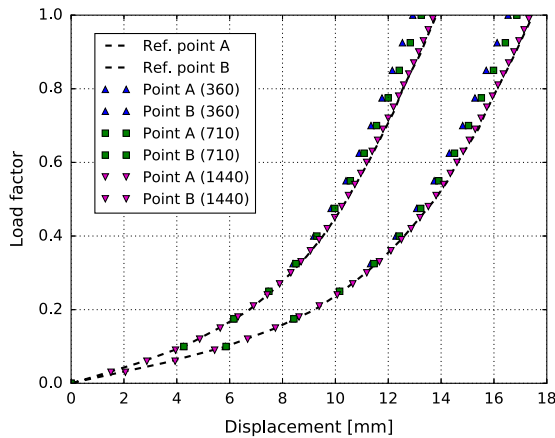
Figure 23. Slit annular plate displacement-load solution.

R = 2540, L = 254
θ = 0.1 radian
h = 12.7 or 6.35
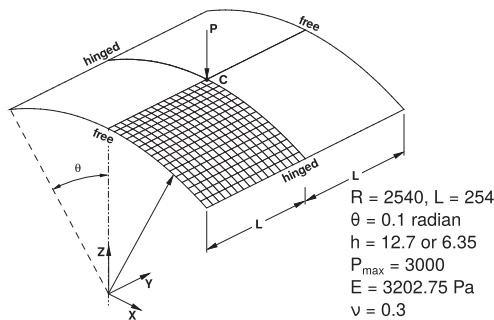P_{max} = 3000
E = 3202.75 Pa
ν = 0.3

Figure 24. Geometry of the hinged cylindrical panel.

A comparison of the results for the coarse mesh (Figure 23) allows to observe the influence of the **ANS** for membrane part that for the maximum load factor indicate a difference in displacements larger than 4%. The results for the fine mesh are in excellent agreement with those provided in Flores (2013b).

3.13. Cylindrical panel test

This example Sze et al. (2004), Flores (2013b) considers a rectangular cylindrical panel simple supported along the straight sides and free along the curved sides, that is subjected to a vertical point load in its centre (see Figure 24). The middle surface geometry is defined by the length of the panel $L = 508$ mm, the radius of the cylinder $R = 2540$ mm and the half angle $\theta = 0.1$ rad. The behaviour of the panel presents a limit point, followed by a strong loss of strength and a final stiffening once the curvature is inverted. Two different thicknesses for the same mid-surface geometry have been considered $t = 12.7$ mm and $t = 6.35$ mm that for the thin case leads to a snap back of the loaded point. This example has been widely used to assess the performance of shell elements and non-linear
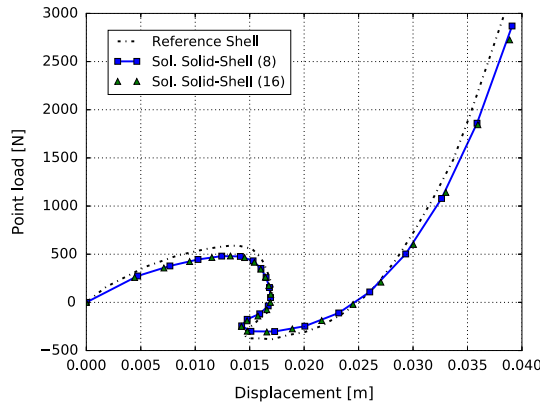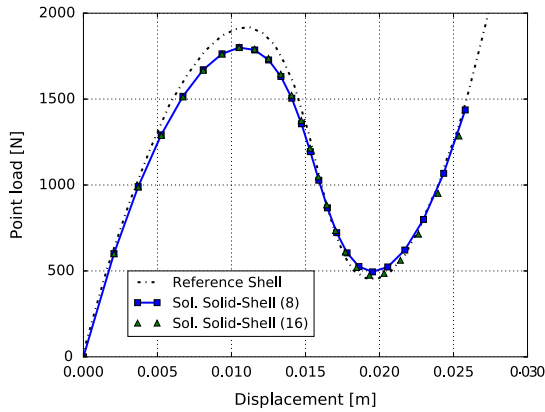
Figure 25. Thin geometry displacement-load.

Figure 26. Thick geometry displacement-load.

Material:
E = 206.9 Pa
ν = 0.29
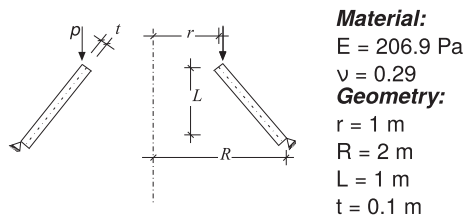**Geometry:**
r = 1 m
R = 2 m
L = 1 m
t = 0.1 m

Figure 27. Initial geometry.

path-following techniques, like the arc-length. For this problem two meshes have been considered with 8 and 16 elements per side. In this case, 2 elements in the thickness direction have been used that allows to introduce the hinge in the middle surface and then to compare with solutions obtained with shell elements. The vertical displacement of the loaded point **C**. Figures 25 and 26 show the evolution of the load-deflection compared with the reference Sze et al. (2004).
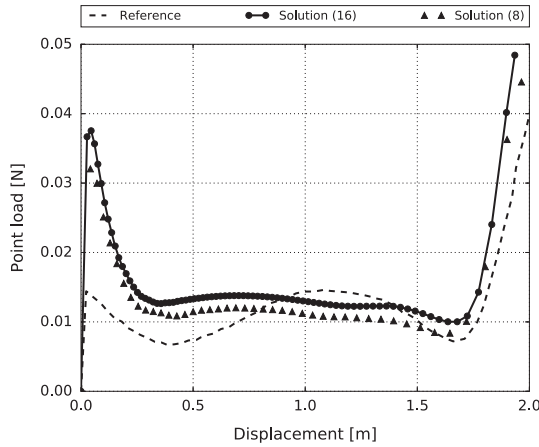
Figure 28. Load-deflection curves.

3.14. Conical shell test

This example is selected to demonstrate the ability of the developed finite element to deal with strongly non-linear situations. The geometrical data are taken from Klinkel et al. (2006). Here, elastic–plastic material behaviour is assumed. All necessary material and geometrical data are depicted in Figure 27. The non-linear behaviour is computed using an arc-length algorithm with displacement control. The constitutive law considered is a J_2 hyperelastic-plastic model with isotropic hardening as a function of the effective plastic strain e^p defined again by (26) and the values of the Table 2.

The results are depicted in Figure 28, where w denotes the vertical displacement of the upper edge. The load deflection diagram demonstrates that our result is close in the order of magnitude to the reference, thus some improvements are needed in the modelisation, in special the relative to the relative to the arc-length strategy.

3.15. Wrinkling test

The problem consists Alexander, Sleight, and Wang (2005), Flores (2013a) of a square membrane (see Figure 29) with side $a = 229$ mm made of a thin film of *Mylar* with thickness $t = 0.0762$ mm. The *Mylar* mechanical properties are $E = 3790$ MPa and $\mu = 0.38$. The top and bottom edges are clamped and the lateral edges are free. The top edge is subjected to a uniform horizontal displacement $\Delta = 1$ mm along the edge.

Two uniform structured mesh with $26 - 26$ and $51 - 51$ nodes, with 1250 and 5000 elements respectively have been considered. Figures 30 and 31 plots two out-of-plane displacement profiles along the centre of the square in both Cartesian directions, as well as the deformation obtained. The solution that we obtain are very close to those obtained in the reference Flores (2013a).
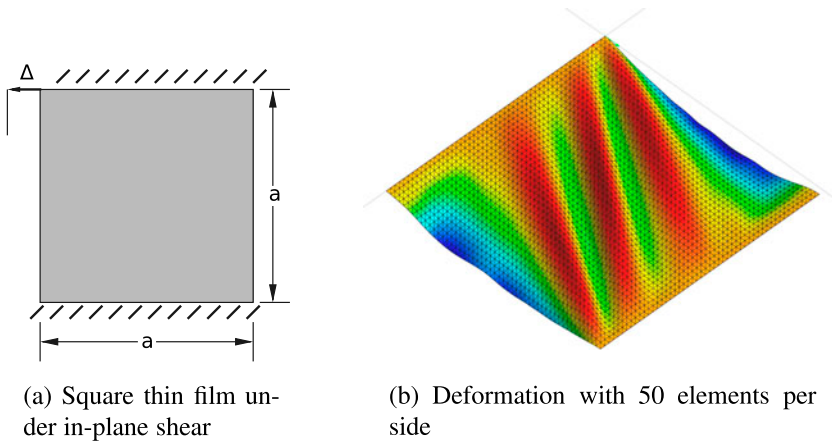
(a) Square thin film under in-plane shear

(b) Deformation with 50 elements per side
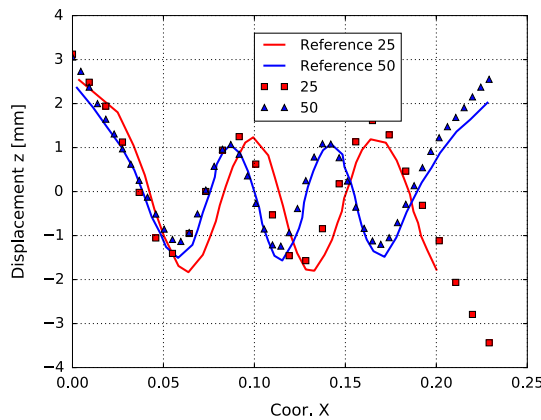
Figure 29. Wrinkling test.

Figure 30. Transverse displacement profiles along the centre of the square: $y = a/2$.

3.16. FSI-Vein test

An additional test that has been performed to check the robustness of the element, which consists in a simple **FSI** (Fluid-Structure Interaction) simulation of an elastic vein. This element has clear advantages from the common approaches performed nowadays, which consist normally in the consideration of multiple layers of solid elements (usually hexahedron), despite the vein is under *shell stresses*. This owing to the need of having a proper and correct definition of the irregular geometry and thickness that a real vein can show, besides a correct definition of the interface for a proper **FSI** simulation, which cannot correctly modelled with a conventional shell element. So this element has advantages of the solid element, and like the element is clearly created to compute *shell stresses* there is no need to consider additional layers of solid to enrich the behaviour of the solid.
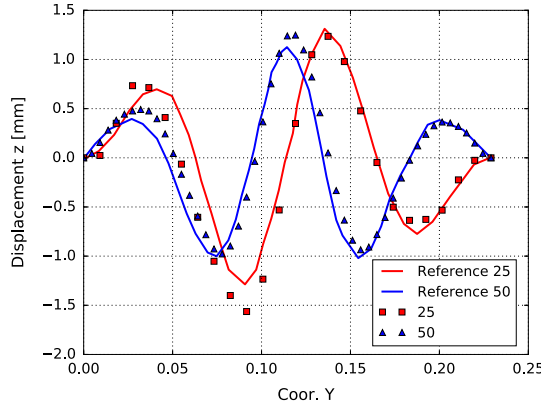
Figure 31. Transverse displacement profiles along the centre of the square: $x = a/2$.

This problem was originally proposed in Nobile (XXXX) and later reproduced in Valdés, Miquel, & Oñate (2009). Its aim is to simulate the **FSI** arising in the modelling of blood flow in human cardiovascular system. As described in Valdés et al. (2009), the problem consists of a thin elastic vessel, which in this case has been modelled with the current element considering an hyperelastic constitutive law, conveying the blood flow, which is modelled as an incompressible fluid using the *Navier-Stokes* equations.

Regarding the geometry, it consists in a straight cylinder of radius $r_0 = 0.005\,\text{m}$ which length and thickness are $L = 0.05\,\text{m}$ and $t = 0.001\,\text{m}$. The blood physical parameters are $\rho_f = 1000\,\text{kg/m}^3$ and dynamic viscosity $\mu_f = 0.003\,\text{kg/ms}$, yielding a kinematic viscosity $\nu_f = 3e - 06\,\text{m}^2/\text{s}$. Regarding the solid parameters, the density is $\rho_s = 1200\,\text{kg/m}^3$ while the *Poisson* ratio and *Young* modulus are $\nu_s = 0.3$ and $E = 3e05\,\text{Pa}$. Regarding the boundary conditions, both sides of the vein are clamped (radial displacements allowed) and an overpressure of $p = 1333.2\,\text{Pa}$ (see (27)) is imposed at the inlet boundary for 3 ms.

$$
p = \begin{cases}
1333.2 \sin\left(2\pi t\right) & \text{if } t \leq 0.25\,\text{ms} \\
1333.2 & \text{if } 0.00025 < t \leq 0.275\,\text{ms} \\
1333.2 \left(1 - \sin\left(2\pi (t - 0.275)\right)\right) & \text{if } 0.275\,\text{ms} < t \leq 0.3\,\text{ms} \\
0.0 & \text{otherwise}
\end{cases} \tag{27}
$$

Figures 32 and 33 collects a comparison between the results in Valdés et al. (2009) and the obtained ones for three control points placed at 0.25, 0.5 and 0.75 l, being *l* the tube length. Regarding the radial displacements (Figure 32), it can be seen that the obtained results are similar to the reference ones. The major differences appear after the peak value when the vein section is recovering its shape. Besides, this vein retraction is much clear in the presented solution and can be clearly noted by the negative radial displacements. This behaviour is more similar to real
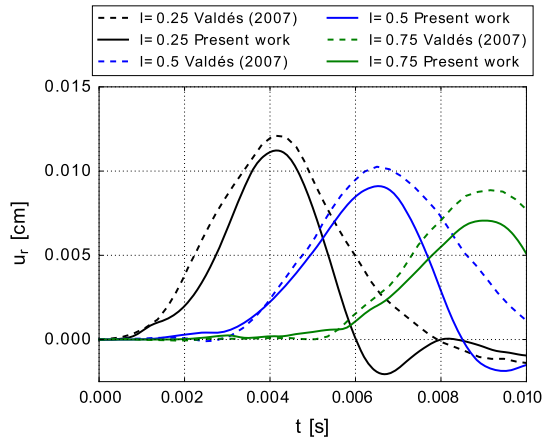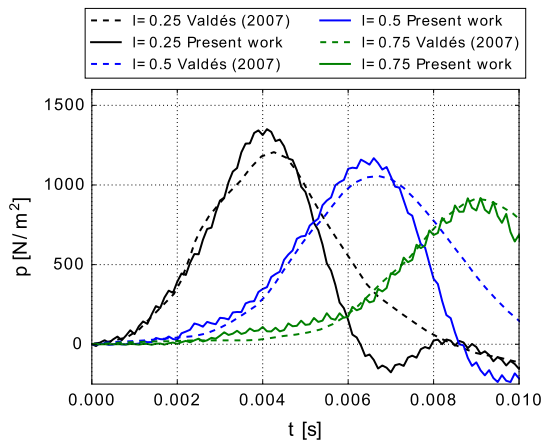
Figure 32. Radial displacement.

Figure 33. Pressure.

hemodynamics and has been also observed in similar problems in the literature (Calvo Plaza, 2006).

On the other hand, the pressure evolution is also assessed in Figure 33. As can be noted, the pressure trend matches the radial displacements evolution but some oscillations appear in the solution. Regarding the nature of these oscillations, it can be asserted that they are not numeric, since one oscillation is developed in several time steps, and this is done due to the fact that any non-reflecting boundary has been considered.

Notes

1. Like in the **EBST** (Flores & Oñate, 2011, 2005; Oñate & Flores, 2005) elements created by *Eugenio Oñate Ibañez de Navarra* and *Fernando G. Flores*.

2. The formulation can be extended to **Updated Lagrangian** following the standard notation, for more information you can look among others (Belytschko, Liu, Moran, & Elkhodary, 2014; de Borst, Crisfield, Remmers, & Verhoosel, 2012).
3. Or nothing more added.
4. If we interpolate the values to the external faces we get $\sigma_{xx} = \sigma_{yy} = \pm 0.6666$ Mpa.
5. Interpolated to the most external faces $\sigma_{xy}\pm = 0.2000$ Mpa.

Acknowledgements

Disclosure statement

ORCID

Vicente Mataix   http://orcid.org/0000-0002-6512-0009
Fernando Flores   http://orcid.org/0000-0002-7567-2691
Riccardo Rossi   http://orcid.org/0000-0003-0528-7074
Eugenio Oñate   http://orcid.org/0000-0002-0804-7095

References

Abed-Meraim, F., & Combescure, A. (2009). An improved assumed strain solid-shell element formulation with physical stabilization for geometric non-linear applications and elastic-plastic stability analysis. *International Journal for Numerical Methods in Engineering, 80*, 1640–1686.

Alexander, T., Sleight, D. W., & Wang, J. T. (2005). Effective modeling and nonlinear shell analysis of thin membranes exhibiting structural wrinkling. *Journal of Spacecraft and Rockets, 42*, 287–298. doi:10.2514/1.3915

Belytschko, T., Liu, W.K., Moran, B., & Elkhodary, K. (2014). *Nonlinear finite elements for continua and structures* (2nd ed.). Chichester: Wiley.

Calvo Plaza, F.J. (2006). *Simulación del flujo sanguíneo y su interacción con la pared arterial mediante modelos de elementos finitos* (PhD thesis). Caminos. Retrieved from http://oa.upm.es/443/

Ribó R, Pasenau M, Escolano E, Ronda JSP. GiD user manual. CIMNE, Barcelona.

Dadvand P, Rossi R, Oñate E. (2010). An object-oriented environment for developing finite element codes for multi-disciplinary applications. Arch Comput Methods Eng, *17*(3):253–297.

de Borst, R., Crisfield, M. A., Remmers, J. J. C., & Verhoosel, C. V. (2012). *Nonlinear finite element analysis of solids and structures* (2nd ed.). Wiley series in computational mechanics. Wiley. Retrieved from http://onlinelibrary.wiley.com/book/10.1002/9781118375938

de Sousa, R. J. A., Cardoso, R. P. R., Valente, R. A. F., Yoon, J.-W., Grácio, J. J., & Jorge, R. M. N. (2005). A new one-point quadrature enhanced assumed strain (EAS) solid-shell element

with multiple integration points along thickness: Part I–geometrically linear applications. *International Journal for Numerical Methods in Engineering, 62*, 952–977.

Dvorkin, E. N., & Bathe, K.-J. (1984). A continuum mechanics based four-node shell element for general non-linear analysis. *Engineering computations, 1*, 77–88.

Flores, F. G. (2013a). A 'Prism' solid element for large strain shell analysis. *Computer Methods in Applied Mechanics and Engineering, 253*, 274–286.

Flores, F. G. (2013b). Development of a non-linear triangular prism solid-shell element using ANS and EAS techniques. *Computer Methods in Applied Mechanics and Engineering, 266*, 81–97.

Flores, F.G. (2013c). Un elementoo prism triangular de sólido-lámina para el análisis de grandes deformaciones. *Mecánica Computacional, XXXII*, 63–87.

Flores, F. G., & Oñate, E. (2011). Wrinkling and folding analysis of elastic membranes using an enhanced rotation-free thin shell triangular element. *Finite Elements in Analysis and Design, 47*, 982–990.

Flores, F. G., & Oñate, E. (2005). Improvements in the membrane behaviour of the three node rotation-free BST shell triangle using an assumed strain approach. *Computer Methods in Applied Mechanics and Engineering, 194*, 907–932. doi:10.1016/j.cma.2003.08.012. Retrieved from http://www.sciencedirect.com/science/article/pii/S004578250400307X

Hauptmann, R., & Schweizerhof, K. (1998). A systematic development of 'solid-shell'element formulations for linear and non-linear analyses employing only displacement degrees of freedom. *International Journal for Numerical Methods in Engineering, 42*, 49–69.

Hauptmann, R., Doll, S., Harnau, M., & Schweizerhof, K. (2001). Solid-shell'elements with linear and quadratic shape functions at large deformations with nearly incompressible materials. *Computers & Structures, 79*, 1671–1685.

Hauptmann, R., Schweizerhof, K., & Doll, S. (2000). Extension of the'solid-shell' concept for application to large elastic and large elastoplastic deformations. *International Journal for Numerical Methods in Engineering, 49*, 1121–1141.

Klinkel, S., Gruttmann, F., & Wagner, W. (2006). A robust non-linear solid shell element based on a mixed variational formulation. *Computer Methods in Applied Mechanics and Engineering, 195*, 179–201. doi:10.1016/j.cma.2005.01.013. Retrieved from http://www.sciencedirect.com/science/article/pii/S0045782505000435

Nobile, F. Numerical approximation of fluid-structure interaction problems with application to haemodynamics. Retrieved from https://infoscience.epfl.ch/record/32934

Oñate, E., & Flores, F.G. (2005). Advances in the formulation of the rotation-free basic shell triangle. *Computer Methods in Applied Mechanics and Engineering, 194*, 2406–2443. Computational methods for shells. doi:10.1016/j.cma.2004.07.039. Retrieved from http://www.sciencedirect.com/science/article/pii/S0045782504005390

Olovsson, L., Unosson, M., & Simonsson, K. (2004). Selective mass scaling for thin walled structures modeled with tri-linear solid elements. *Computational Mechanics, 34*, 134–136. doi:10.1007/s00466-004-0560-6

Parente, M., Valente, R. F., Jorge, R. N., Cardoso, R., & de Sousa, R. J. A. (2006). Sheet metal forming simulation using EAS solid-shell finite elements. *Finite Elements in Analysis and Design, 42*, 1137–1149. doi:10.1016/j.finel.2006.04.005. Retrieved from http://www.sciencedirect.com/science/article/pii/S0168874X06000783

Schwarze, M., & Reese, S. (2011). A reduced integration solid-shell finite element based on the EAS and the ANS concept – Large deformation problems. *International Journal for Numerical Methods in Engineering, 85*, 289–329.

Schwarze, M., Vladimirov, I. N., & Reese, S. (2011). Sheet metal forming and springback simulation by means of a new reduced integration solid-shell finite element technology. *Computer Methods in Applied Mechanics and Engineering, 200*, 454–476.

Sena, J., Alves de Sousa, R., & Valente, R. (2011). On the use of EAS solid-shell formulations in the numerical simulation of incremental forming processes. *Engineering Computations, 28*, 287–313.

Sena, J. I., Lequesne, C., Duchene, L., Habraken, A.-M., Valente, R. A., & Alves de Sousa, R. J. (2016). Single point incremental forming simulation with adaptive remeshing technique using solid-shell elements. *Engineering Computations, 33*, 1388–1421.

Sze, K., Liu, X., & Lo, S. (2004). Popular benchmark problems for geometric nonlinear analysis of shells. *Finite Elements in Analysis and Design, 40*, 1551–1569. doi:10.1016/j.finel.2003.11.001. Retrieved from http://www.sciencedirect.com/science/article/pii/S0168874X0300218X

Valdés, J.G., Miquel, J., & Oñate, E. (May 2009). *Nonlinear finite element analysis of orthotropic and prestressed membrane structures* (PhD thesis), Universitat Politècnica de Catalunya, Amsterdam, The Netherlands: doi:10.1016/j.finel.2008.11.008

Wang, P., Chalal, H., & Abed-Meraim, F. (2016). Quadratic solid-shell elements for nonlinear structural analysis and sheet metal forming simulation. *Computational Mechanics, 59*, 1–26. Retrieved from https://link.springer.com/article/10.1007/s00466-016-1341-8

Appendix 1. Pull-back, push-forward fundamental concepts

In this appendix, we introduce the concepts of **pull-back** and **push-forward** necessaries to understand the concepts introduced previously, the main reference for this has been taken from Belytschko et al. (2014). These operations allow us to have an unified description between the *Eulerian* and *Lagrangian* tensors. In (A1) we can appreciate some examples.

A push-forward by $\mathbf{F}$ of the *Lagrangian* vector $d\mathbf{X}$ to the current configuration gives the *Eulerian* vector $d\mathbf{x}$:

$$d\mathbf{x} = \mathbf{F} \cdot d\mathbf{X} \equiv \phi_* d\mathbf{X} \tag{A1a}$$

The pull-back by $\mathbf{F}^{-1}$ of the *Eulerian* vector $d\mathbf{x}$ to the reference configuration gives $d\mathbf{X}$.

$$d\mathbf{X} = \mathbf{F}^{-1} \cdot d\mathbf{x} \equiv \phi^* d\mathbf{x} \tag{A1b}$$

where ϕ_* and ϕ^* represent the **push-forward** and **pull-back** operations respectively.

If we extend these operations, we can consider the **pull-back** and **push-forward** operations on second-order tensors to obtain the relationships between these tensors in the deformed and undeformed configurations. These concepts provide us a mathematically consistent method for defining the time derivatives of the tensors, called **Lie-derivatives**. Considering all this, the operations can be considered for example to obtain a formulation of **hyperelastic-plastic** constitutive model based on the multiplicative decomposition of the deformation gradient, for more information consult (Belytschko et al., 2014).